Additive Manufacturing 32 (2020) 101106

Contents lists available at ScienceDirect

Additive Manufacturing

journal homepage: www.elsevier.com/locate/addma

Full Length Article

Additive manufacturing of two-phase lightweight, stiff and high damping carbon fiber reinforced polymer microlattices★

Zhenpeng Xu[a], Chan Soo Ha[b], Ruthvik Kadam[b], John Lindahl[c], Seokpum Kim[c], H. Felix Wu[d], Vlastimil Kunc[c], Xiaoyu Zheng (Rayne)[a,b,*]

[a] Department of Civil and Environmental Engineering, Department of Mechanical and Aerospace Engineering, University of California, Los Angeles, CA 90095, USA
[b] Department of Mechanical Engineering, Virginia Tech, Blacksburg, VA 24061, USA
[c] Manufacturing Demonstration Facility, Oak Ridge National Laboratory, Oak Ridge, TN 37831, USA
[d] Vehicle Technologies Office, U.S. Department of Energy, 1000 Independence Ave., SW, Washington, DC, 20585, USA

ARTICLE INFO

Keywords:
Carbon fiber reinforced polymer
Multi-material additive manufacturing
Stereolithography
Cellular material
Damping

ABSTRACT

Carbon fiber reinforced polymer (CFRP) composite is known for its high stiffness-to-weight ratio and hence is of great interest in several engineering fields such as aerospace, automotive, defense, etc. However, such a composite is not suitable for energy dissipation as failure occurs with very little or no plastic deformation. Herein, we present an extendable multi-material projection microstereolithography process capable of producing carbon-fiber-reinforced cellular materials that achieve simultaneously high specific stiffness and damping coefficient. Inspired by the upper bounds of stiffness-loss coefficient in a two-phase composite, we designed and additively manufactured CFRP microlattices with soft phases architected into selected stiff-phase struts. Our results, confirmed by experimental and analytical calculations, revealed that the damping performance can be significantly enhanced by the addition of only a small fraction of the soft phase. The presented design and additive manufacturing strategy allow for optimizing mutually exclusive properties. As a result, these CFRP microlattices achieved high specific stiffness comparable to commercial CFRP, technical ceramics, and composites, while being dissipative like elastomers.

1. Introduction

Recent progress in additive manufacturing (AM) technologies has enabled the realization of 3D architected metamaterials with extraordinary mechanical and structural properties, including ultralight weight [1,2], high stiffness and strength [3,4], negative Poisson ratio [5], and damage tolerance [6,7]. However, combinations of lucrative properties are unattainable, limited by their single material composition [8–12]. For example, lightweight lattice materials made from ceramics have high stiffness and strength but are not desirable for energy dissipation [11,13]; on the other hand, elastomeric materials have a high damping coefficient but are not suitable for structural applications [14]. Lately, CFRP composites and lattices have been of great interest in automotive [15], aerospace [16,17], and research [18–21] applications due to their high stiffness and light weight. However, as with other stiff materials, CFRP composites suffer from poor damping, which limits their application for energy dissipation. While several fiber-reinforced composites additively manufactured by the fused filament fabrication process [22–27] and other techniques [28–31] have been well-studied, there are few reports on achieving complex 3D lattice structures with feature sizes lower than a few hundred micrometers, limiting their potential for precision components and property space design.

Herein, we present an extendable multi-material PμSL process,

Abbreviations: CFRP, carbon fiber reinforced polymer; PμSL, projection microstereolithography; AM, additive manufacturing; DMD, digital micromirror device; DMA, dynamic material analysis; FOM, figure of merit

* Corresponding author at: 420 Westwood Plaza, University of California, Los Angeles, CA 90095, USA.
E-mail address: rayne@seas.ucla.edu (X. Zheng).

https://doi.org/10.1016/j.addma.2020.101106
Received 6 December 2019; Received in revised form 30 January 2020; Accepted 31 January 2020
Available online 01 February 2020
2214-8604/

capable of producing CFRP lattice materials that achieve simultaneously high specific stiffness and damping coefficient. Using this multi-material photo-polymerization, a class of CFRP lattice materials with predesigned stiff and soft phases can be formed. Inspired by two-phase composite theory where the arrangement of soft inclusions within a stiff phase defines the bounds of stiffness-damping pairs, we designed and additively manufactured low-density lattice materials with a fraction of soft phase embedded within stiff CFRP strut members. This design allows tuning and optimizing the effective stiffness and the loss tangent (i.e., a measure of damping) by varying the volume fractions of two constituent materials. In addition, we found that the Reuss configuration allows the achievement of the upper bound of specific stiffness and damping pairs of the composites. To investigate the damping performance of the microlattices, dynamic material analysis (DMA) and quasi-static cyclic compression tests were performed at small and large strains, respectively. Our results, confirmed by experimental and analytical calculations, revealed that both intrinsic (at small strains) and structural (at large strains) damping performance, quantified by a figure of merit (FOM), $E^{1/3}\tan\delta/\rho$, where E is the effective compressive Young's modulus, $\tan\delta$ is the effective loss tangent, and ρ is the microlattices density [1], were significantly enhanced by the addition of only a small volume fraction of the soft phase. For design usefulness, we created tunability maps describing the damping performance of the microlattices as a function of the selected design parameters. These CFRP microlattices achieved high specific stiffness comparable to commercial CFRP, technical ceramics, and composites, while being dissipative like elastomers. The presented work points to a direction where mutually exclusive properties can be simultaneously achieved via multi-material additive manufacturing.

2. Materials and methods

2.1. Materials and resin preparation

An ultraviolet (UV) curable CFRP composite, made of a UV sensitive resin reinforced with short carbon fibers, was developed for the fabrication. The matrix materials contained methacrylated monomers and oligomers (Formlabs Rigid, Formlabs Inc). A photo-initiator, phenylbis (2,4,6-trimethylbenzoyl) phosphine oxide (Sigma-Aldrich Inc), was added to the fiber-matrix mixture for photopolymerization. The fibers were obtained from E&L Enterprises, Inc (PC100). A high-energy ball mill was used to mix the monomer, photo-initiator, and carbon fiber (up to 20 vol% loading). This mixing method ensured a uniform spatial distribution of the fibers (see Appendix Fig. A1). A dissipative phase, comprised of methacrylate monomers and oligomers (Formlabs Flexible, Formlabs Inc), was prepared as the second phase to be added during the multi-material additive manufacturing process.

Resins reinforced by different fiber loadings were formulated. These resins after curing exhibited higher stiffness than that of the base monomer, with the measured tensile stiffness increased from 2.47 GPa to 3.02 GPa with an addition of 5 vol% of fibers (per ASTM D3039). The fibers after mixing had a diameter of 5 μm, and an average length of 68 μm (measured by ZEISS SteREO Discovery.V20). We measured the viscosity of the resin loaded by a range of carbon fiber loadings at room temperature via the rheometer, and it showed that its viscosity rapidly increased with the increase of fiber loading. (Appendix Table A2).

2.2. Multi-material additive manufacturing of two-phase materials

Based on the work of D. Chen et al. [5,32,33], a multi-material PμSL system that could print viscous multiple resins via a recoating fixture and a material switching system was designed and built, as shown in Fig. 1(a). To fabricate a multi-material part, a CAD model was sliced into different groups of closely spaced images such that each group represented one material. These two-dimensional slices were subsequently digitized and sent to a digital micromirror device (DMD) chip which projected an image at 405 nm wavelength through a series of lenses onto the corresponding photosensitive resin. This process initiated polymerization of the resin, converting it into a solid single layer part that had the same shape as the projected images. Each cured layer was followed by a recoating process in which the build platform was raised, allowing the resin to settle for the next layer. The recoating process for CFRP composite was achieved by the doctor blade which will be discussed later. When the other material needed to be fabricated in the same layer or the next layer, the translation stage moved the washing vat to the position of the platform, and the previously printed part was cleaned by a cleaning dispenser. After cleaning, the platform moved to the other resin vat to print the next layer.

2.3. Recoating process and cure depth characterizations of highly vicious CFRP composite

To process highly viscous fiber-loaded resin ($\mu \sim 7.8$ Pa.s), we developed a recoating fixture employing the tape-casting technique [13,34] to ensure the viscous resin was efficiently recoated as shown in Fig. 1(b). Firstly, a small amount of CFRP composite was extruded onto the oxygen-permeable window. Then, a doctor blade was moved from left to right, spreading the resin on the window. The blade had a speed of $V = 5$ mm/s relative to the window. The distance between blade and window δ_{blade} was controlled to ensure that the resin's height was high enough, and it could spread to the whole printing area. The thickness of the coating layer δ_{coating} was half of δ_{blade}. Moreover, to guarantee each layer could be fully cured, δ_{coating} was set as $\delta_{\text{coating}} > k\delta$ ($k > 1$), where δ is the layer thickness and k is the safety factor. The recoating quality of different fiber loading resins was tested (Appendix Fig. A2), and we observed that the maximum fiber loading that yielded a layer with good quality was approximately 20 vol%. For the resin that had fiber loading more than 20 vol%, the fibers massed into clusters during the recoating process, making the resin non-printable.

To quantify the working curve for each loaded resin, a relationship between the curing depth and the exposure energy was characterized to locate the optimal exposure parameters; the working curve for the resin with 20 vol% fiber loading is given in Appendix Fig. A3(b). The measured working curve confirmed that the curing depth was linearly proportional to the natural logarithm of the UV exposure energy, which showed good agreement with the analytical model represented by $Z_{cd} = (1/\alpha) \cdot \ln(E/E_c)$ where α is the resin absorption coefficient, E is the actual energy of light and E_c is the critical exposure energy required to initiate polymerization [35]. E was controlled by the UV light intensity and the exposure time, and E_c was controlled by the resin inherent property.

2.4. Post-processing and fabricated samples

Our PμSL system was designed to achieve a minimum printable 3D feature size of ~50 μm in the projection plane. This was determined by the pixel resolution of the DMD array and the printing area. The resolution in the vertical direction was determined by a driving motor, which was 5 μm, and we set the layer thickness as 40 μm. After printing, all samples were cleaned with ethanol and post-cured using UV light. This process was followed by thermal post-cure at 150 °F for 24 h. To demonstrate the capabilities of our technique, samples with complex 3D structures at the millimeter-scale were fabricated, as shown in Fig. 1(c) and (d). Fig. 1(e) shows a multi-material octet-truss unit cell comprising of CFRP composite and polyethylene glycol diacrylate resin, and Fig. 1(g) and (h) show a gyroid structure with a minimum feature size of 150 μm. The process is not limited to the dimensions demonstrated in microlattices here, while it can be extended to samples of tens of centimeters or larger as shown in Fig. 1(f).

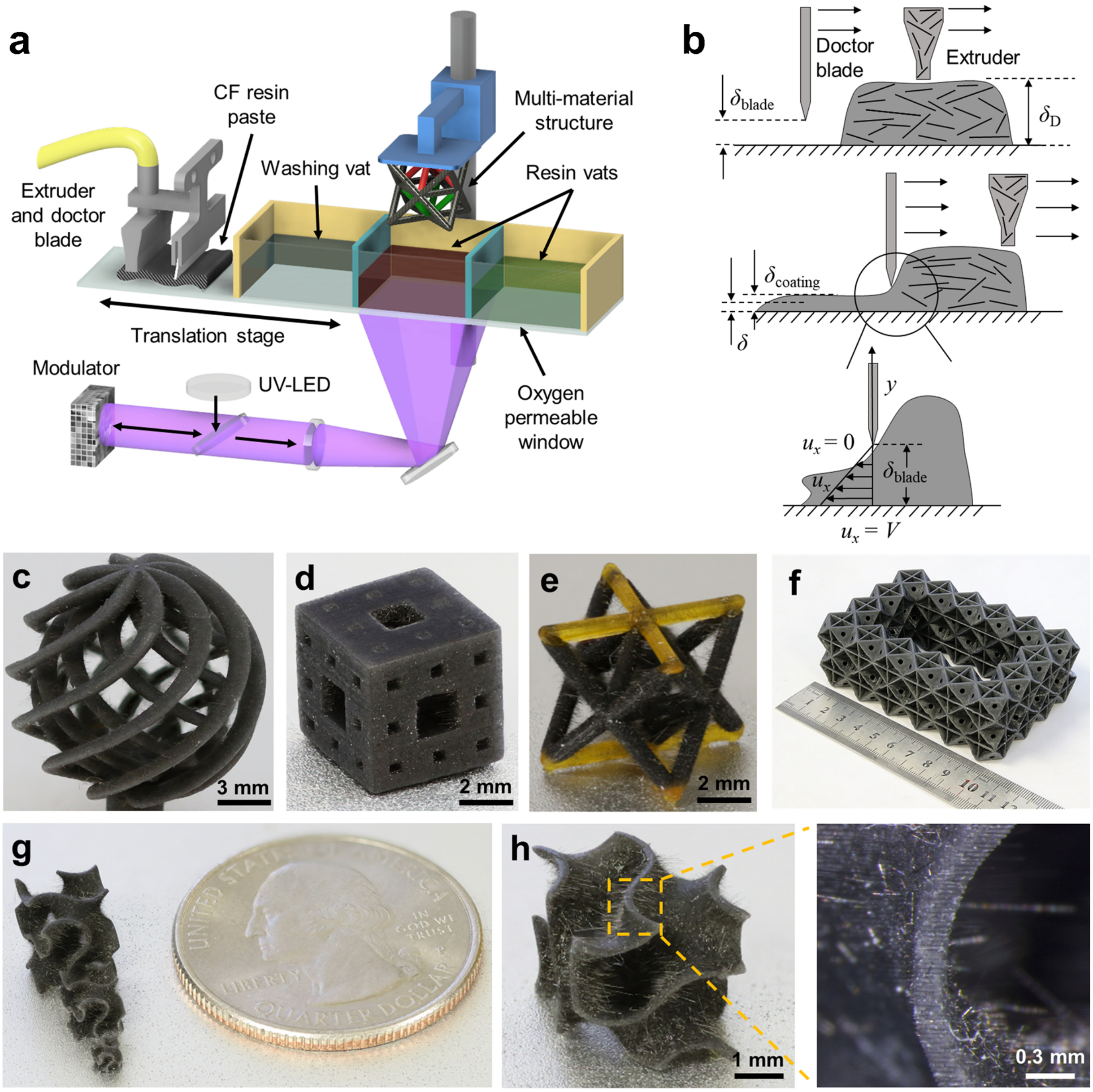

Fig. 1. Customized multi-material microstereolithography (PμSL) system and fabricated samples. (a) Schematic of multi-material PμSL process integrated with the tape-casting method. (b) Schematic of the recoating process. (c)-(d) Complex 3D structures fabricated by the system. (e) A multi-material octet-truss unit cell comprising of carbon fiber reinforced polymer composite and polyethylene glycol diacrylate resin. (f) A closed-cell lattice with a dimension over tens centimeters. (g–h) Gyroid 3D structure with a wall thickness of 150 μm.

2.5. Energy dissipation characterizations

The energy dissipation mechanism of the as-fabricated CFRP microlattices was quantified through their small and large strains deformations, considering both intrinsic and structural damping from the multi-phase material and designed micro-architectures.

To capture intrinsic damping properties at small strains, we performed DMA tests using TA Instruments DMA 850. All tests were performed with a maximum strain of 0.05 % to ensure that all fabricated samples were excited elastically at small strains. Although a frequency sweep was performed from 0.1 Hz to 20 Hz, the results measured at 0.1 Hz were selected for a direct comparison of loss tangent from small-strain DMA and large-strain cyclic compression tests, since the frequency of quasi-static compression testing is usually considered to be less than 0.1 Hz [36].

Structural damping properties at large strains were investigated by quasi-static cyclic compression tests using an INSTRON 5944 test frame equipped with Bluehill data acquisition software and a 2000 N load cell. A strain rate of 10^{-3} 1/s was adopted to ensure that all samples deform quasi-statically (i.e., to suppress mass inertia effect). Load-displacement curves were collected by the software linked to the test frame and were converted into engineering strain and stress via $\varepsilon = \delta/L_0$ and $\sigma = P/A$, where P and δ are the load and displacement measured by the load cell, L_0 is the initial length, and A is the effective cross-section area. This conversion provided a stress-strain hysteresis loop, and the effective stiffness was obtained from the slope of the linear elastic region in the loading section. Dissipated energy ΔU (area within the loop) and the stored energy U (area under the loading curve) were calculated, respectively. The loss coefficient Ψ, defined as the ratio of the dissipated energy to the stored energy (i.e., $\Psi = \Delta U/U$), was then computed and converted to the loss tangent via $\tan\delta = 2\Psi/\pi$ [14,36,37]. This process was necessary for a direct comparison of the loss tangent at small and large strains. Note that this relationship represents a quarter-cycle of a full compressive loading-unloading cycle [14].

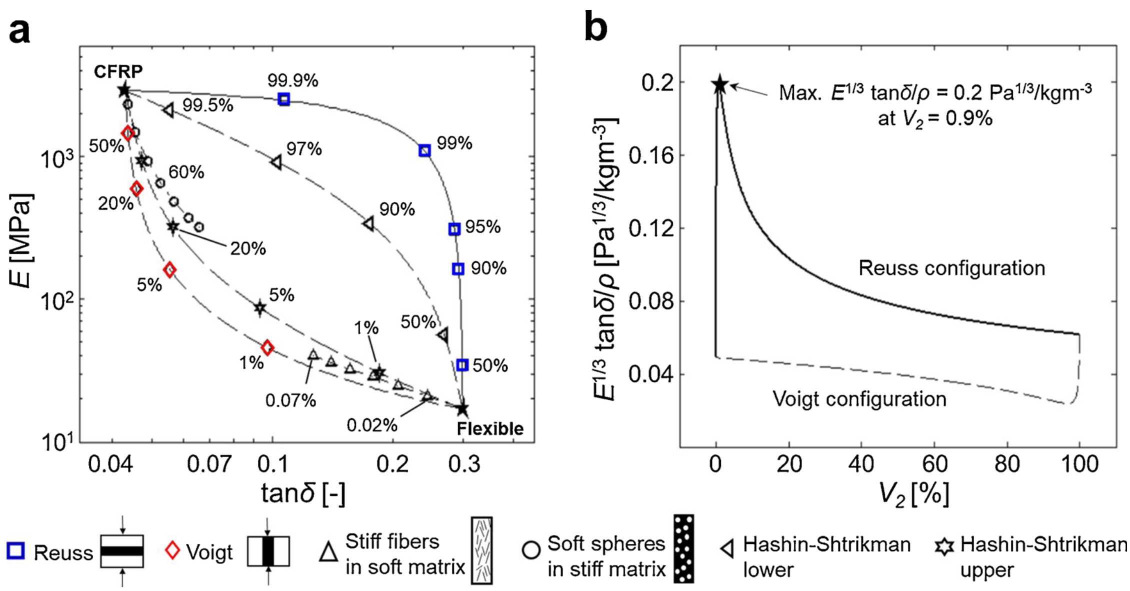

Fig. 2. The effect of soft phase on the bulk CFRP stiffness-damping properties. (a) Stiffness (E) vs. loss tangent (tanδ) for various two-phase configurations incorporating CFRP and soft phase of bulk material. The percentage shown here corresponds to the volume fraction of the stiff phase (V_1). Graphical legends are provided at the bottom of this figure. (b) $E^{1/3}$tanδ/ρ versus the volume fraction of the soft phase (V_2). This index has its maximum at V_2 = 0.9 %.

3. Theory and hypothesis

Despite brittleness from the nature of stiff CFRP composites, it is promising that a two-phase composite layout incorporating the CFRP composites with a soft phase can lead to high stiffness-loss efficiency. To determine the effects of the soft phase on the bulk CFRP stiffness-damping properties, we performed an analytical study of several representative two-phase layouts by varying volume fraction of the soft phase and computed their effective stiffness (equivalent to storage modulus, E) and loss tangent based on two-phase composite theory [14,38]. Fig. 2(a) illustrates an E-tanδ relationship of different layouts; the percentage in this figure corresponds to the volume fraction of phase 1. The layouts considered here included Reuss and Voigt composites, Hashin-Shtrickman composites, stiff fibers in a soft matrix, and soft spheres in a stiff matrix. Here, phase 1 (stiff phase) was the CFRP composite (5 vol% fiber loading), and phase 2 (soft phase) was a soft elastomer; the material properties of these phases can be found in Appendix Table B1. Analytical expressions of the stiffness and damping for these layouts can be found in Appendix C. Our calculations show that a small volume fraction of phase 2 in the Reuss composite led to a substantial increase in loss tangent with a reasonable reduction in stiffness. Conversely, the Voigt composite required a substantial addition of phase 2 to achieve an appreciable increase in loss tangent. The upper and lower bounds of Hashin-Shtrickman composites were bounded by those of the Voigt and Reuss composites, respectively, and the stiff fibers- and soft spheres- inclusion composites behaved similarly to the Voigt composite.

Since the Reuss and Voigt layouts represented the upper and lower bounds in the stiffness-loss relationship in our study, we assessed these two layouts to identify the volume fraction of phase 2 that maximizes damping performance in terms of the damping FOM, $E^{1/3}$tanδ/ρ. This material index is intended for plate- or panel-shaped applications for energy absorption, and it expresses how fast a clamped plate subject to forced vibrations reaches rest when the forcing term is removed, applicable to applications of lattice materials for damping management [36,39–41]. The lightest material for the plate or panel application is that with the highest value of $E^{1/3}/\rho$ [39,42]. As depicted in Fig. 2(b), the Reuss layout having a volume fraction of phase 2 equal to approximately 0.9 % was found to exhibit a maximal FOM. Therefore, the Reuss layout is a pertinent framework to design a structure with high stiffness-damping efficiency.

4. Results and discussion

4.1. Design and production of two-phase CFRP microlattices

The above rationales provide conceptual design guidelines to optimize the stiffness-damping efficiency for two-phase bulk composites, then we extend these principles to a class of lightweight high stiffness lattice topologies [1,43]. Here, we developed lightweight CFRP microlattices consisting of periodically arrayed octet-truss unit cells in which the soft phase is embedded in selected out-of-plane struts, as shown in Fig. 3(a). The octet-truss topology was chosen as a repeating unit cell in the microlattices because its deformation mechanism is stretching-dominated which gives rise to a favorable stiffness-to-weight ratio compared to stochastic bending-dominated cells [1,3,43]. The soft phase was then intentionally inserted at the center of the selected struts to increase the maximum global strain, which in turn enlarges the area of stress-strain hysteresis loop leading to an improved energy absorption performance.

The soft phase ratio in the octet-truss unit cell, V_{soft}, defined as the ratio of h to H, controls the volumetric material distribution between the CFRP composite and the soft phase, which tailors the stiffness-damping property of the microlattice. Here, $V_{soft}^{lattice} = (2/3)V_{soft}$, where $V_{soft}^{lattice}$ denotes the ratio of the soft phase volume to the entire microlattice's volume, since the Reuss layout presents only in the selected out-of-plane struts. The relative density of the microlattice, $\bar{\rho}$, is approximated by $\bar{\rho} = 6\pi\sqrt{2}\,(r/l)^2$, where r is the strut radius and l is the strut length [43,44]. The microlattice's density equals to the product of its relative density and base material's density.

To investigate the damping performance of the present microlattice, unit cells (3 for each density group) having a range of relative densities ($\bar{\rho}$ ~ 4 %, 7 %, 12 %) and soft phase ratios (V_{soft} ~ 0 %, 5 %, 9 %, 13 %, 20 %) with a side length of 15 mm were fabricated using the multi-material PμSL system. Fig. 3(b) depicts an as-fabricated 3-3-3 lattice sample having $\bar{\rho}$ = 7 % with V_{soft} = 9 % as an example. The interface between the soft and stiff phase is covalently bonded after radical photopolymerizations, and was experimentally confirmed to be adequately strong to transfer tensile and compression loads to adjacent layers. As shown in Fig. 3(c), a scanning electron microscope (SEM) image was taken at the interface of the CFRP and soft phase.

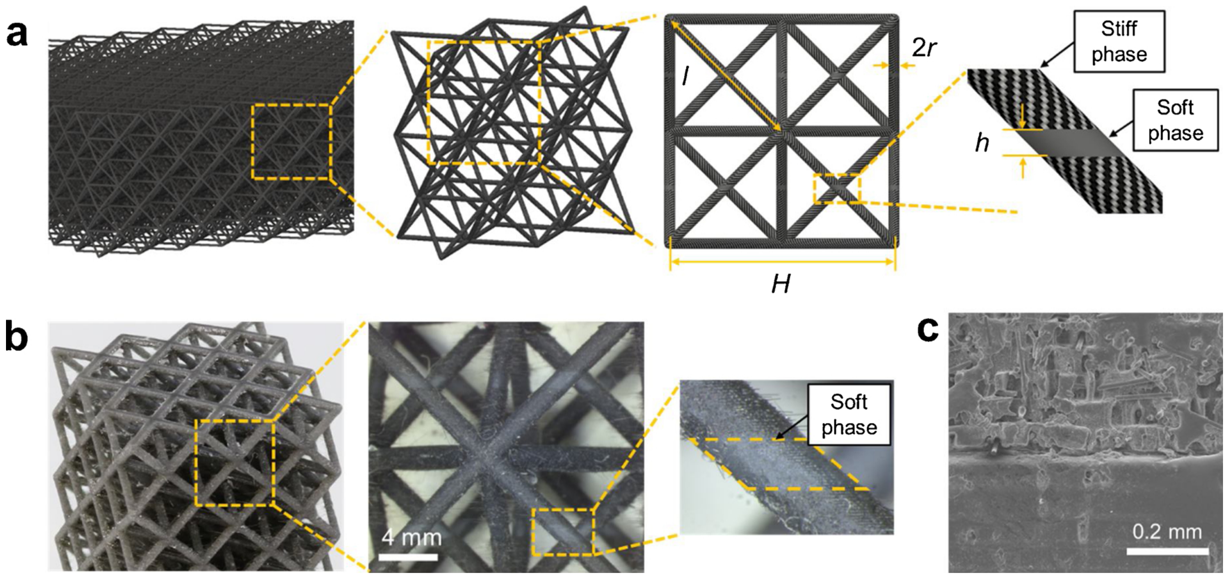

Fig. 3. Multi-material architecture. (a) Design of lightweight, stiff, high damping microlattice with two-phase materials incorporating CFRP and soft phase. (b) Fabricated lightweight cellular CFRP microlattice having $\bar{\rho}$ = 7 % with V_{soft} = 9 %. (c) SEM image showing the interface between the two phases, where the top section is CFRP and the bottom section is soft phase.

4.2. Intrinsic damping at small strains

Fig. 4(a) and (b) show the measured modulus and loss tangent of samples with a range of soft phase ratios, obtained by DMA tests. These values were averaged over three test results, and error bars represent the standard deviation. Here, we only considered the relative density of 7 % since the intrinsic damping was invariant with respect to the relative density [14], and this was verified by our analytical model (Appendix C). We observed that the effective modulus of the samples showed an exponential relationship as a function of V_{soft} via $E = a{\cdot}\exp(b{\cdot}V_{soft}) + c{\cdot}\exp(d{\cdot}V_{soft})$ (coefficients are provided in Appendix B).

Conversely, intrinsic damping tanδ was nonlinearly proportional to V_{soft} via $\tan\delta = a{\cdot}\exp(b{\cdot}V_{soft}) + c$ (coefficients are provided in Appendix B). A trendline approaches an asymptotic value of the loss tangent to be approximately 0.32, which corresponds to the inherent loss tangent of the soft phase. Moreover, the loss tangent reaches its asymptotic value earlier than the modulus at a given change in V_{soft}. For example, the magnitude of the modulus at V_{soft} = 9 % is still a factor of approximately 2 times larger than that at V_{soft} = 20 % (from 6.13 MPa to 2.66 MPa), whereas the magnitude of the loss tangent at V_{soft} = 20 % was approximately 1.2 times larger than that at V_{soft} = 9 % (from 0.267 to 0.32). This result is consistent with the theoretical response of a bulk Reuss composite illustrated in Fig. 2(a), which implies that the design rules for bulk composites can be applied to these two-phase lattice materials at small strains.

We further investigated the stiffness-damping performance of our designed microlattices by the damping FOM, defined as $E^{1/3}\tan\delta/\rho$ in the previous section. The FOM was calculated using the measured effective modulus and loss tangent values to identify the optimal soft phase percentage, as shown in Fig. 4(c). A solid line represents a curve fit of the damping FOM. The computed value reaches its peak when V_{soft} was equal to approximately 10 %, which was approximately a factor of 2 times larger than a similar microlattice but made of CFRP composite entirely.

4.3. Structural damping at large strains

Stress-strain hysteresis loops of samples with $\bar{\rho}$ = 4 % and $\bar{\rho}$ = 12 % having V_{soft} = 20 % in response to multicyclic compression (30 cycles) are shown in Fig. 5(a) and (b), respectively. We observed that the hysteresis loops stabilized after the first three cycles, which implies the presence of non-recoverable mechanisms such as localized nodal fractures and possible inelastic deformation. The loss coefficient, Ψ, monotonically decays with cycle number in which a reduction of approximately 25 % was seen after the first three cycles (see insets in these figures). In Fig. 5(c), the evolution of the stress-strain hysteresis loop is presented over different relative densities ($\bar{\rho}$ = 4 %, 7 %, 12 %) while holding V_{soft} constant (V_{soft} = 20 %). To adequately display this evolution, we normalized both stress and strain of the loops with respect to their maximum values. Dominant deformation mechanism at a

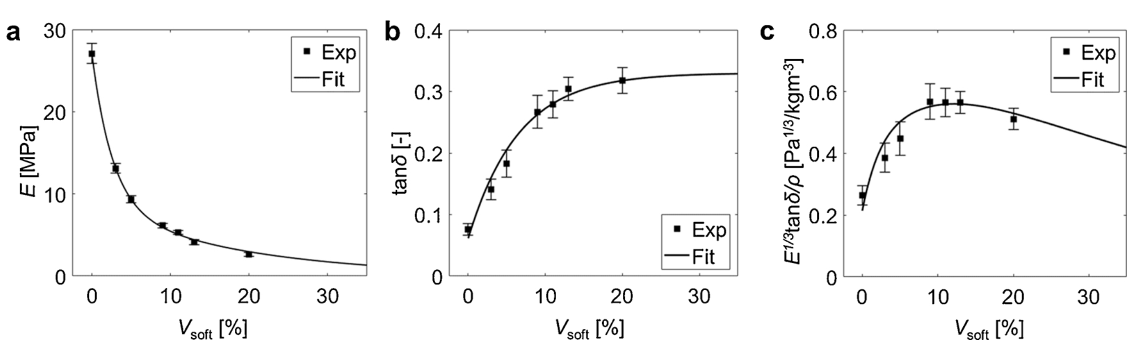

Fig. 4. Intrinsic damping properties of the lightweight cellular CFRP microlattices having a relative density of 7 % with different soft phase ratios. The values were averaged over three test results, and error bars represent the standard deviation. Solid lines in these figures represent the curve fit. (a) The effective modulus (E) as a function of the soft phase ratio V_{soft}. (b) Loss tangent (tanδ) as a function of V_{soft}. (c) Damping FOM as a function of V_{soft}.

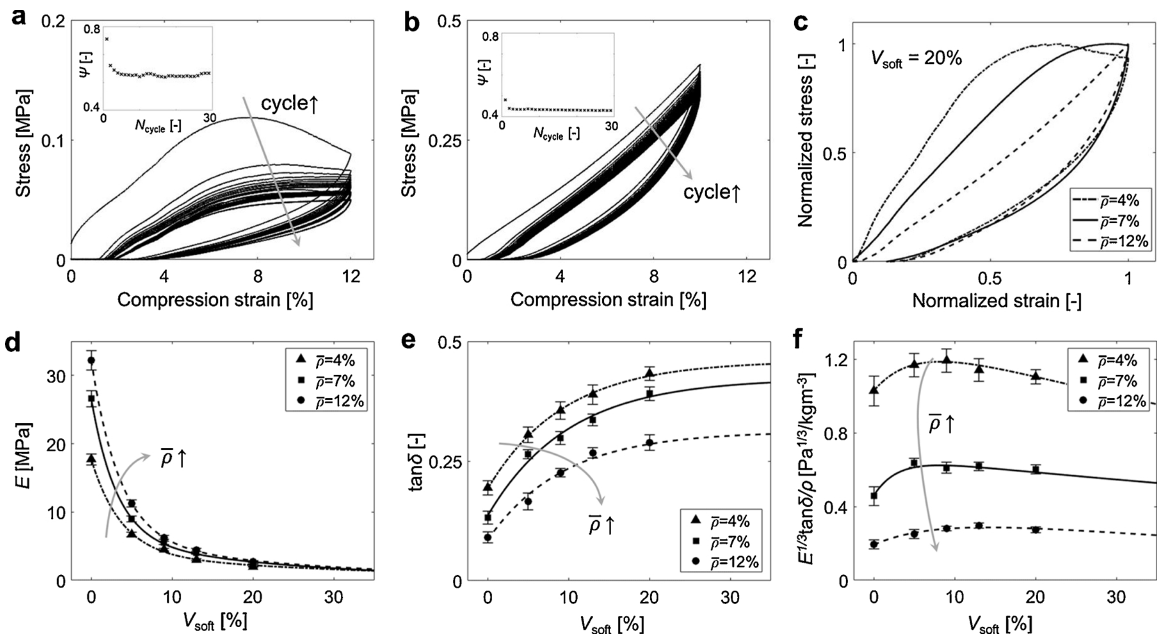

Fig. 5. Structural damping properties of the lightweight cellular CFRP microlattices obtained from large strains quasi-static cyclic compression tests. (a)-(b) Hysteresis loops from multicyclic compression tests for 30 cycles and evolution of the loss coefficient with cycle number. (a) Sample with $\bar{\rho}$ = 4 % having V_{soft} = 20 %. (b) Sample with $\bar{\rho}$ = 12 % having V_{soft} = 20 %. (c) Normalized stress-strain hysteresis loops of samples having V_{soft} = 20 % with various $\bar{\rho}$. (d) The effective modulus as a function of V_{soft} for different relative densities. (e) Loss tangent (tanδ) as a function of V_{soft} for different relative densities. (f) Damping FOM as a function of V_{soft}, showing its maximum at different V_{soft} for different relative densities. In (d)-(f), the values were averaged over three test results, and error bars represent the standard deviation.

low relative density ($\bar{\rho}$ = 4 %) was elastic buckling of the constituent struts, however, this buckling response diminished with an increase in the relative density ($\bar{\rho}$ = 7 %), and plastic yielding mechanism started to dominate deformation at a higher relative density ($\bar{\rho}$ = 20 %). This difference in deformation mechanisms at different relative densities affects the shape of the stress-strain hysteresis loops that in turn leads to a change in the dissipated energy per cycle.

We observed that the measured modulus decreases monotonically with an increase in V_{soft}, and this relationship is nearly identical to one observed from intrinsic properties (Fig. 5(d)). This is because the modulus is a mechanical property that is invariant to the magnitude of global strains according to the nature of elasticity. Curve fits for the measured modulus were found to follow an exponential relationship with V_{soft} (see Appendix B for more details). Structural loss tangent of the microlattices, computed via tanδ = 2Ψ/π, is shown in Fig. 5(e). The structural loss tangent increases monotonically with V_{soft} but decreases with relative density. Additionally, the loss tangent reaches its asymptotic value with an increase in V_{soft}, and this convergence is more rapid for samples with higher relative densities. Our finding implies that a cellular structure is preferable to a bulk material for structural damping. Structural damping FOM was calculated and plotted in Fig. 5(f). The results showed that the maximum FOM for different relative densities occurs at different V_{soft}. For example, samples having $\bar{\rho}$ of 4 % and 7 % showed such peaks when V_{soft} ~ 6 %, whereas a peak for a sample having $\bar{\rho}$ of 12 % occurs when V_{soft} is equal to approximately 12 %.

4.4. Discussion

Fig. 6 illustrates the tunability maps of intrinsic and structural damping FOM using the measured data and polynomial fittings in the V_{soft} vs. $\bar{\rho}$ space. This map allows the designer to choose the volume fraction of the soft phase and the relative density for the desired FOM. The FOM for both intrinsic and structural damping has its maximum at low relative densities and at the soft phase ratio ranging approximately from 6 % to 12 %.

A specific stiffness vs. loss tangent ($E^{1/3}$/ρ — tanδ) map was created to quantitatively assess the performance of the stiffness-damping pair of our CFRP microlattices against other existing materials (CES EduPack 2018, Granta Design [45]) for vibrational management (Fig. 7) [39,41,42]. The envelope defined by all experimental results is highlighted by an orange ellipse in $E^{1/3}$/ρ vs. tanδ material space. We discovered that the CFRP microlattices have a specific stiffness comparable to commercially available CFRP composites while being dissipative like elastomers. For instance, the microlattices exhibit similar $E^{1/3}$/ρ to that of technical ceramics and other composites and achieves improved damping by almost two orders of magnitude in loss tangent tanδ.

Additionally, we compared the measured stiffness-damping properties of the CFRP microlattices with analytical calculations at small strain deformations (See Appendix C). The mechanical behaviors between the model and experimental results for a relative density of 7 % as a function of soft phase ratio V_{soft} were compared as an example (Fig. C2 and Table C1). The experimentally observed effective modulus trendline agrees well with analytical estimation. We observed a slightly larger discrepancy in intrinsic loss tangent vs. V_{soft} trendline, which is attributed to the challenges to obtain accurate control of the soft phase ratio especially when V_{soft} was below 5 %.

5. Conclusions

We presented an extendable tape-casting-integrated multi-material PμSL process capable of producing cellular CFRP materials with simultaneously high specific stiffness and damping coefficient. Our process is capable of incorporating multiple resins with disparate mechanical properties and high viscosity, allowing direct additive manufacturing of materials and components comprised of combinations of different stiffness and damping pairs. The presented lightweight CFRP microlattices achieved the upper bound of stiffness and damping pairs of a composite via a Reuss layout where soft phase sections were inserted into stiff struts in the microlattices. DMA tests and quasi-static cyclic compression tests at small and large strains confirmed that a small fraction of the soft phase (~ 6 %) was capable of dramatically increasing both intrinsic and structural damping performance of the microlattices. The creation of a tunability map for vibrational management allowed us to choose the optimal FOM, ($E^{1/3}$tanδ/ρ), via

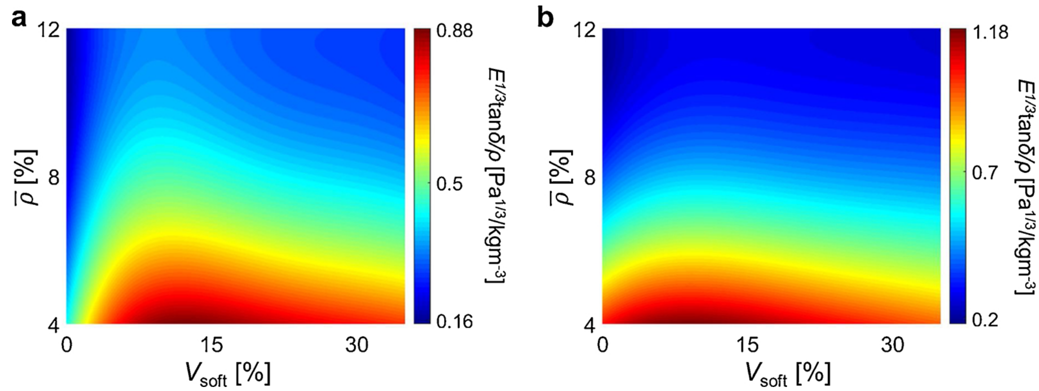

Fig. 6. Tunability maps for (a) intrinsic and (b) structural damping performance in terms of the damping FOM obtained from experimental measurements.

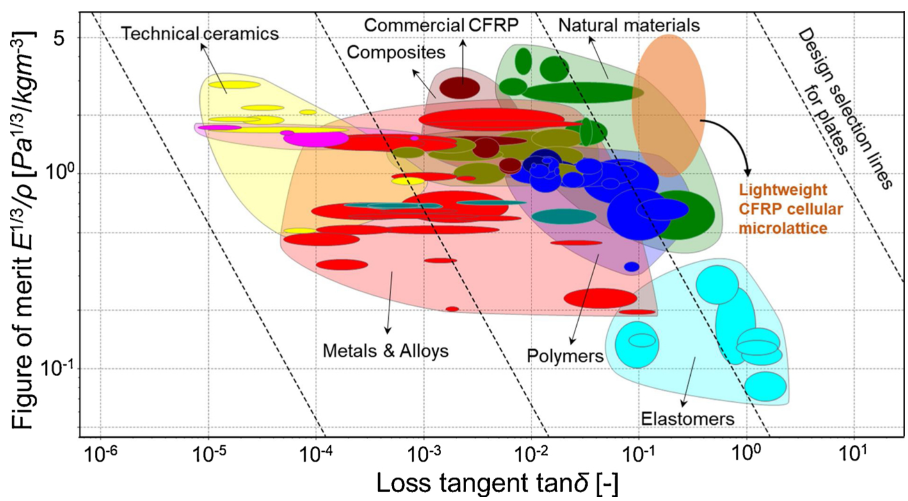

Fig. 7. Assessment of vibration management of plates. The lightweight cellular CFRP microlattices developed in this work are compared against all existing natural and manmade materials in a log-log graph. The orange ellipse represents the envelope of all experimental results.

combinations of relative density and soft phase ratio. Our results indicated that these microlattices with architected stiff and soft phases exhibit a comparable specific stiffness to commercial CFRP while being dissipative like elastomers.

Author contributions

X. Zheng conceived and designed the research. Z. Xu carried out additive manufacturing system setup and performed polymerization experiments and measurement. C. Ha developed the design of the two-phase CFRP microlattice and performed the analytical calculations. Z. Xu and R. Kadam fabricated samples and performed the tests. C. Ha, Z. Xu and R. Kadam analyzed the data. Z. Xu wrote the initial draft of the manuscript. Z. Xu, C. Ha, and R. Kadam finalized the manuscript with input from all authors. V. Kunc, *J.* Lindahl, and S. Kim contributed to carbon fiber synthesis and dynamic property measurement. The technical assistance of R. Hensleigh, H. Cui, K. Jung, and M. Hemminger is greatly appreciated.

CRediT authorship contribution statement

Zhenpeng Xu: Methodology, Software, Validation, Formal analysis, Investigation, Data curation, Writing - original draft, Writing - review & editing, Visualization. **Chan Soo Ha:** Methodology, Software, Formal analysis, Writing - review & editing, Writing - original draft, Visualization. **Ruthvik Kadam:** Software, Validation, Formal analysis, Investigation, Writing - review & editing. **John Lindahl:** Investigation, Resources. **Seokpum Kim:** Resources, Writing - review & editing. **H. Felix Wu:** Project administration, Writing - review & editing. **Vlastimil Kunc:** Resources, Project administration, Funding acquisition. **Xiaoyu Zheng:** Resources, Conceptualization, Writing - review & editing, Writing - original draft, Supervision, Project administration, Funding acquisition.

Declaration of Competing Interest

The authors declare no conflict of interest.

Acknowledgements

This work is sponsored by the U.S. Department of Energy, Office of Energy Efficiency and Renewable Energy, Vehicle Technologies Program, under contract DE-AC05-00OR22725 with UT-Battelle, LLC (4000162266). C. Ha, R. Kadam and X. Zheng would also like to thank the AFOSR Air Force Office of Scientific Research (FA9550-18-1-0299) and Office of Naval Research (N00014-18-1-2553) for financial support.

Appendix A. Material

Table A1

Table A1
Formulations of the CFRP resins.

Fiber loading [vol%]	Weight of carbon fiber [g]	Volume of monomer [ml]	Weight of initiator [g]
5	4.45	47.50	1.71
10	8.90	45.00	1.62
20	17.80	40.00	1.44

Table A2
Viscosity testing results of the CFRP resins.

Fiber loading [vol%]	Viscosity [Pa-s]
0	1.786
5	2.025
10	2.483
20	7.803

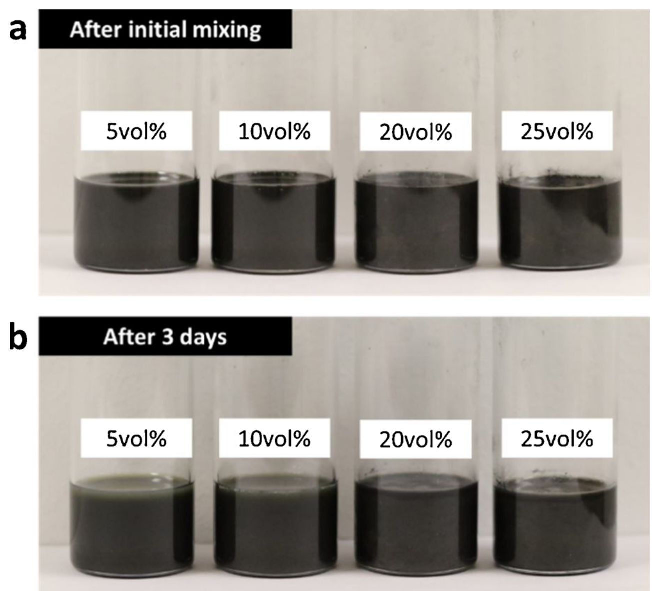

Fig. A1. Optical images of the resins mixed with different carbon fiber loadings. (a) After initial mixing. (b) After 3 days. The resins are stable, and the sediment phenomenon is not obvious.

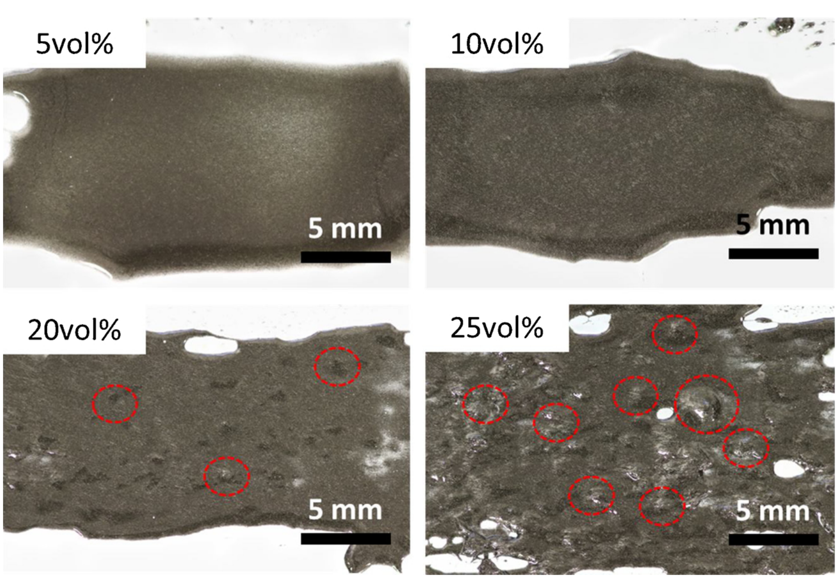

Fig. A2. Optical images of CFRP composite resin films with different fiber loadings after recoating. Circled area refers to a piece of dense cluster of massed fibers. While there are some clusters in 20 vol% resin film, it is still can be used for the fabrication. However, the situation becomes severe when fiber loading goes to 25 vol%, making the recoating process harder.

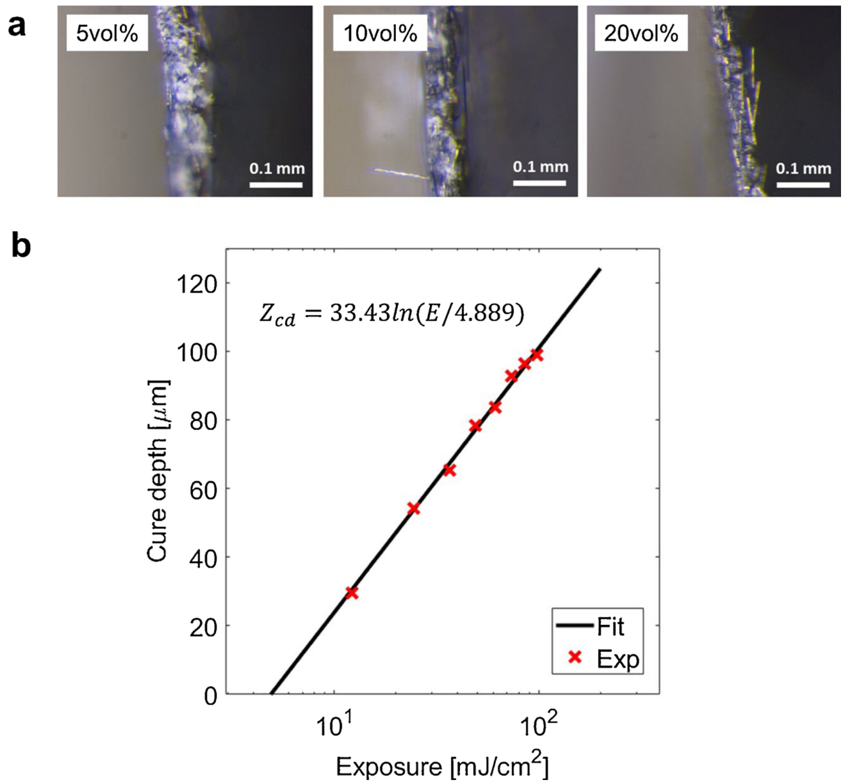

Fig. A3. (a) Optical images of single cured layer for 5 vol%, 10 vol%, 20 vol% fiber loading resins with 5 s exposure time. (b) Curing depth of the 20 vol% loading resin as a function of the exposure energy.

Appendix B. Experimental setup and result

The damping capacity of a material is often defined as loss tangent (tanδ). In the field of viscoelasticity, δ is called the phase (or loss) angle (or shift) between stress and strain sinusoidal responses and is a measure of the loss angle of a linearly viscoelastic material. This angle also represents the width of the elliptic Lissajous figure [14]. The procedure to determine the tanδ of the bulk sample is as follows. First, a compression or tension film clamp was used to load the sample onto a DMA apparatus (TA Instruments DMA 850). A nitrogen tank attached to the DMA test frame was used to regulate the temperature. Once the desired temperature (25° in Celsius) was reached, a strain sweep was carried out from 0.01 % strain to 10 % strain at a frequency of 1 Hz to determine the maximum strain within the elastic region for the sample (per ASTM D5026). This method is destructive because the sample must enter its plastic region as the strain increases and becomes permanently deformed. Thus, this plastically deformed sample was replaced with a new sample. The new sample was loaded with a frequency sweep from 0.1 Hz to 20 Hz to measure its tanδ. Within this range, the results at 0.1 Hz was adopted because the corresponding tanδ allows for a direct comparison with structural damping property obtained from the quasi-static cyclic compression tests since a frequency of such tests is in general below 0.1 Hz [36]. The fiber loading of all tested samples is 5 vol%. The measured material property is listed in Table B1.

Table B1
Bulk material properties.

Material	Storage modulus [MPa]	Loss modulus [MPa]	tanδ [-]
CFRP	2717.6	184.7	0.068
Flexible	7.4	2.2	0.299

We measured 3 samples at each point and took the average of a data set. Error bars in the stiffness and damping figures refer to the standard deviation which is calculated by the equation $s = \sqrt{\frac{\sum_{i=1}^{n}(x-\bar{x})^2}{n-1}}$. The standard deviation of the FOM, $\frac{E^{1/3}\tan\delta}{\rho}$, is calculated by the error propagation equation, $s_{\mathrm{FOM}} = \sqrt{\frac{1}{9}(s_{\mathrm{s}})^2 + (s_{\mathrm{d}})^2}$, where s_{s} and s_{d} are the standard deviation of stiffness and damping. The test data after averaging and curve fitting are provided below.

Storage modulus and intrinsic damping of samples, representing the lightweight CFRP cellular microlattices with a relative density of 7 %, is provided in Table B2. We performed the curve fit on these measured mechanical properties using $E = a{\cdot}\exp(b{\cdot}V_{\mathrm{soft}}) + c{\cdot}\exp(d{\cdot}V_{\mathrm{soft}})$ and $\tan\delta = a{\cdot}\exp(b{\cdot}V_{\mathrm{soft}}) + c$ to see their trends, and the coefficients of the curve fits are listed in Table B3.

Table B2
Storage modulus (i.e., stiffness), intrinsic damping and corresponding standard deviation (*SD*) of the samples with a relative density of 7 % at small strains.

V_{soft}	0 %	3 %	5 %	9 %	11 %	13 %	20 %
Storage modulus [MPa]	27.060	13.112	9.323	6.130	5.320	4.108	2.659
tanδ [-]	0.076	0.141	0.183	0.267	0.279	0.304	0.318
$SD_{storage\_modulus}$ [MPa]	1.218	0.577	0.438	0.294	0.208	0.337	0.242
$SD_{\tan\delta}$ [-]	0.009	0.017	0.023	0.028	0.023	0.019	0.021

Table B3
The coefficients of fitting equations of storage modulus (i.e., stiffness) and loss coefficient of the samples with a relative density of 7 % at small strains.

Coefficients	*a*	*b*	*c*	*d*	R^2
Storage modulus [MPa]	18.43	−38.22	8.62	−5.36	0.9989
tanδ [-]	−0.27	15.37	0.33	n/a	0.9711

Stiffness and loss coefficients of the samples at large strains are listed in Tables B4 and B5. These measured properties were curve fitted via $E = a{\cdot}\exp(b{\cdot}V_{soft}) + c{\cdot}\exp(d{\cdot}V_{soft})$ and $\tan\delta = a{\cdot}\exp(b{\cdot}V_{soft}) + c$. The coefficients of the curve fits are provided in Tables B6 and B7.

Table B4
Stiffness and corresponding standard deviation (*SD*) in [MPa].

$\bar{\rho}$ \ V_{soft}	0 %	5 %	9 %	13 %	20 %
4 %	17.725	6.720	4.510	3.012	1.988
7 %	26.597	8.969	5.510	4.004	2.337
12 %	32.213	11.250	6.250	4.440	2.740
$SD_{4\%}$	0.798	0.229	0.239	0.069	0.131
$SD_{7\%}$	1.011	0.413	0.314	0.092	0.096
$SD_{12\%}$	1.546	0.315	0.219	0.120	0.090

Table B5
Structural loss coefficients and corresponding standard deviation (*SD*) [unitless].

$\bar{\rho}$ \ V_{soft}	0 %	5 %	9 %	13 %	20 %
4 %	0.305	0.479	0.558	0.611	0.679
7 %	0.207	0.415	0.468	0.527	0.614
12 %	0.142	0.260	0.310	0.419	0.453
$SD_{4\%}$	0.015	0.016	0.018	0.020	0.014
$SD_{7\%}$	0.014	0.009	0.014	0.012	0.015
$SD_{12\%}$	0.011	0.017	0.009	0.011	0.016

Table B6
The coefficients of fitting equations of modulus of samples.

$\bar{\rho}$ \ Coefficients	*a*	*b*	*c*	*d*	R^2
4 %	13.84	−27.14	3.86	−2.93	0.9992
7 %	20.58	−31.89	6.00	−4.07	0.9987
12 %	26.37	−28.28	5.84	−3.66	0.9999

Table B7
The coefficients of fitting equations of loss coefficient of samples.

$\bar{\rho}$ \ Coefficients	*a*	*b*	*c*	R^2
4 %	−0.27	10.71	0.46	0.9967
7 %	−0.29	10.06	0.42	0.9880
12 %	−0.23	10.75	0.31	0.9889

Appendix C. Analytical model

Analytical model for bulk two-phase composites

In Section 3 of the main text, we studied the E-tanδ relationship of representative two-phase bulk composite layouts made of a soft (viscoelastic) phase and a stiff (CFRP composites) phase. In the field of viscoelasticity [14], their moduli are complex and are expressed as $E^* = E' + iE''$, where E' denotes the storage modulus and E'' denotes the loss modulus. In addition, the loss tangent tanδ, by definition, is related via the ratio of the imaginary to real parts of E^* (i.e., $\tan\delta = E''/E'$).

According to the viscoelastic correspondence principle [14], for Reuss composite layout comprising phase 1 (stiff) and phase 2 (soft), the complex modulus can be expressed as $E^*_{\text{Reuss}} = \left[\frac{f}{E_1^*} + \frac{1-f}{E_2^*}\right]^{-1}$, where f represents the volume fraction of phase 1, and E_1^* and E_2^* denote the complex moduli of phase 1 and 2, respectively. Then, its effective modulus (storage modulus) and loss tangent of the Reuss composite can be expressed as:

$$E_{\text{Reuss}} = \text{Re}(E^*_{\text{Reuss}}) \tag{C.1}$$

$$\tan\delta_{Reuss} = \frac{(\tan\delta_1 + \tan\delta_2)(f + (1-f)(E_1'/E_2')) - (1 - \tan\delta_1\tan\delta_2)(f\tan\delta_2 + (1-f)\tan\delta_1(E_1'/E_2'))}{(1 - \tan\delta_1\tan\delta_2)(f + (1-f)(E_1'/E_2')) + (\tan\delta_1 + \tan\delta_2)(f\tan\delta_2 + (1-f)\tan\delta_1(E_1'/E_2'))} \tag{C.2}$$

where E_1' and E_2' represent storage moduli of phase 1 and 2, respectively, and tanδ_1 and tanδ_2 denote the loss tangent of phase 1 and 2, respectively. Similarly, for Voigt composite layout, the complex modulus is $E^*_{\text{Voigt}} = E_1^* f + E_2^*(1-f)$. Then, the effective modulus (storage modulus) and loss tangent of Voigt layout can be expressed as:

$$E_{\text{Voigt}} = \text{Re}(E^*_{\text{Voigt}}) \tag{C.3}$$

$$\tan\delta_{\text{Voigt}} = \frac{f\tan\delta_1 + (1-f)(E_2'/E_1')\tan\delta_2}{f + (1-f)(E_2'/E_1')} \tag{C.4}$$

Detailed analytical expressions of the stiffness and damping for other layouts can be found in Ref. [14,38].

Analytical model for the two-phase CFRP microlattice at small strains

Intrinsic damping is associated with material properties due to the nature of viscoelasticity; that is, such damping is not caused by large deformation mechanisms such as buckling which most likely appears in large strains. In order to obtain intrinsic material properties of the microlattice, we first determined the effective modulus of a unit cell creating the microlattice in quasi-static conditions at small strains. Here, we considered axial, bending, and shear forces applied on the constituent struts of octahedron-tetrahedron (i.e., octet-truss) cells. Such a topology is stretch-dominated; hence one may consider axial stress only since bending and shear stress are relatively small as compared to axial stress. However, this would not be a case for the microlattices presented in our study because their out-of-plane struts were made of two dissimilar materials complying with the Reuss layout, which may cause the microlattice deforms differently due to macro/micro-frictions at interfaces of the two materials and their intrinsic viscoelastic effects. To accommodate this, we adopted Timoshenko's beam theory, and hence our analysis includes every aspect of axial, bending, and shear deformation mechanisms. In addition, we assumed an infinite microlattice in this analysis. With these assumptions, we first derived the stiffness and loss tangent for the cell made of a homogeneous material. Consider an out-of-plane strut of the octahedral cell (i.e., the core of the octet-truss cell), as shown in Fig. C.1 . We defined an effective length L_{eff} ($L_{\text{eff}} = L_{\text{strut}} - 2r$) to take into account the nodal volume effect, where r is the radius of circular cross-sections; that is, mass accumulation at the nodes is considered. Note that the Reuss layout is not illustrated in this figure for simplicity. When subjected to a unidirectional compressive loading, both ends of the strut move due to axial compression and bending. Due to the axial compression, the corresponding axial displacement is

$$\delta_{\text{A}} = \frac{F_{\text{A}} L_{\text{eff}}}{E_{\text{s}} A} \tag{C.5}$$

where E_{s} is an elastic modulus of a base material that makes the cell and A is the cross-sectional area of the strut. To determine displacements due to bending and shear of the strut, we then obtained moment M_{s} and shear force F_S along the strut at position s according to the Timoshenko beam theory

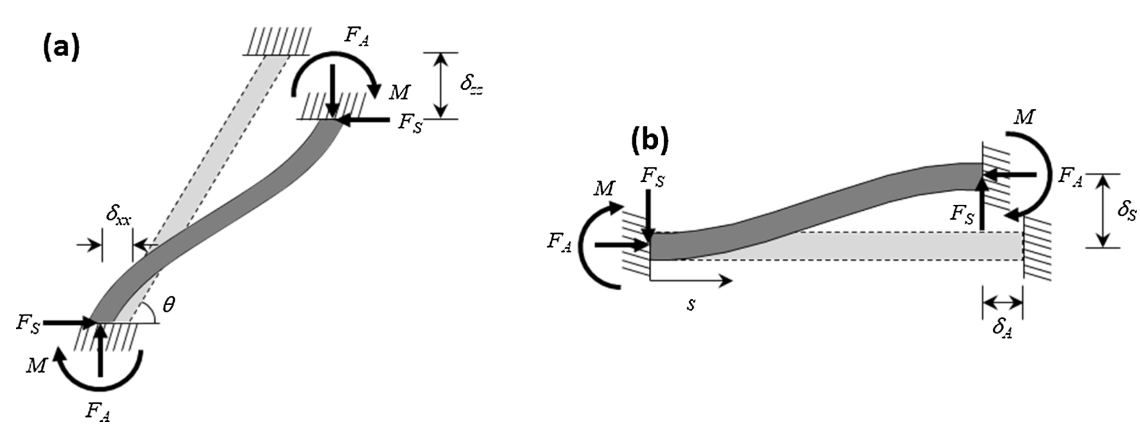

Fig. C1. Schematics of the deformation of the out-of-plane strut of the lightweight cellular CFRP microlattice under uniaxial compression. Loading state in (a) the global coordinate, (b) the local coordinate.

as follows.

$$M_s = E_s I \frac{\partial \varphi}{\partial s} \tag{C.6a}$$

$$F_S = \kappa A G_s (\frac{\partial w}{\partial s} - \varphi) \tag{C.6b}$$

where I is the second moment of inertia, ϕ is the strut rotation, and κ is Timoskenko shear coefficient ($\kappa = \frac{6(1+\nu)}{7+6\nu}$ for solid circular cross-section, and $\kappa = \frac{10(1+\nu)}{12+11\nu}$ for solid rectangular cross-section, where ν is Poisson's ratio), G_s is the shear modulus of the base material, w is a deflection of the strut at position s. Note that for a Timoshenko beam, $\frac{\partial \omega}{\partial s} \neq \varphi$ due to the shear effect as opposed to that of the Euler-Bernoulli beam theory. From a force equilibrium, an expression of M_s can be easily expressed as

$$M_s = \frac{1}{2} F_S L_{\mathrm{eff}} - F_S s \tag{C.7}$$

By imposing boundary condition, that is $\varphi(s{=}0) = 0$, and integrating Eq. (C.6a) using Eq. (C.7), we obtain

$$\varphi = \frac{F_S L_{\mathrm{eff}}}{2E_s I} s - \frac{F_S}{2E_s I} s^2 \tag{C.8}$$

Substituting Eq. (C.8) into (C.6b) and integrating with respect to s yields

$$w(s) = \frac{F_S s}{\kappa A G} + \frac{F_S}{2E_s I}(\frac{1}{2} L_{\mathrm{eff}} s^2 - \frac{1}{3} s^3) \tag{C.9}$$

Applying boundary condition at $s = L_{\mathrm{eff}}$, the displacement due to shear and bending can be finally obtained as:

$$\delta_S = w(s = L_{\mathrm{eff}}) = \frac{F_S L_{\mathrm{eff}}}{\kappa A G} + \frac{F_S L_{\mathrm{eff}}^3}{12 E_s I} \tag{C.10}$$

From Eqs. (C.5) and (C.10), the axial force F_A and the shear force F_S applied to the strut are then expressed as:

$$F_A = \frac{E_s A}{L_{\mathrm{eff}}} \delta_A \tag{C.11a}$$

$$F_S = \left[\frac{L_{\mathrm{eff}}}{\kappa A G} + \frac{L_{\mathrm{eff}}^3}{12 E_s I}\right]^{-1} \delta_S \tag{C.11b}$$

The strain energy stored in the strut, considering axial, bending, and shear deformations, can be expressed as:

$$U_{\mathrm{out-of-plane}} = \frac{1}{2} F_A \delta_A + \int_0^{l'} [M_S \frac{\partial \varphi}{\partial s} + F_S (\frac{\partial w}{\partial s} - \varphi)] ds \tag{C.12}$$

Using Eqs. (C.7)–(C.9), and (C.13), Eq. (C.12) can be simplified as:

$$U_{\mathrm{out-of-plane}} = \frac{\pi E_s r^2 \delta_A^2}{2 L_{\mathrm{eff}}} + \frac{6 C_1 E_s I \delta_S^2}{L_{\mathrm{eff}}^3} \tag{C.13}$$

where $C_1 = \left[\frac{12 E_s I}{\kappa A G L_{\mathrm{eff}}^2}\right]^{-1}$ and $G = \frac{E_s}{2(1+\nu)}$. Note that the equation above represents the total strain energy stored in the out-of-plane strut.

The strain energy for the in-plane strut, which is only subjected to tension, is simply:

$$U_{\mathrm{in-plane}} = \frac{\pi E_s r^2 \delta_x^2}{2 L_{\mathrm{eff}}} \tag{C.14}$$

where δ_x represents the displacement of the strut in the global x-axis. The relationships between the strut and the global coordinates in terms of displacements are

$$\delta_z = \delta_D \cos\theta + \delta_A \sin\theta \tag{C.15a}$$

$$\delta_x = \delta_D \sin\theta + \delta_A \cos\theta \tag{C.15b}$$

For the octet-truss configuration, a strut inclination angle θ is 45°. Using Eq. (C.15), Eq. (C.13) can be re-written as:

$$U_{\mathrm{out-of-plane}} = \frac{\pi E_s r^2}{2 L_{\mathrm{eff}}} (-\delta_x + \delta_z)^2 + \frac{6 C_1 E_s I}{L_{\mathrm{eff}}^3} (\delta_x + \delta_z)^2 \tag{C.16}$$

Assuming $\delta_x = \frac{1}{3}\delta_z$ and circular cross-section struts, Eqs. (C.10) and (C.12) can be further simplified as

$$U_{\mathrm{out-of-plane}} = \frac{\pi r^2 E_s}{9} [\frac{1}{L_{\mathrm{eff}}} + 12 C_1 \frac{r^2}{L_{\mathrm{eff}}^3}] \delta_z^2 \tag{C.17a}$$

$$U_{\mathrm{in-plane}} = \frac{\pi E_s r^2}{9 L_{\mathrm{eff}}} \delta_z^2 \tag{C.17b}$$

Although the relationship between the axial and vertical displacements (i.e., $\delta_x = \frac{1}{3}\delta_z$) is valid for pin-joined struts [44], it is pertinent to use such an approximation because relative densities considered in our work is relatively very low ($\bar{\rho} < 12$ %) in which nodal effects due to fixed joints are negligible. Note that Eq. (C.17) represents the strain energy for the out-of-plane and the in-plane struts that are made of a homogeneous material.

For the octahedral cell consisting of 4 in-plane struts made solely of CFRP composite and 8 out-of-plane struts made of CFRP composite and soft phase complying the Reuss layout as appeared in our design, we needed to substitute the modulus with $E_s = E^*_{\text{Reuss}}$ in Eq. (C.17a) and $E_s = E_{\text{CF}}$ in Eq. (C.17b), where $E^*_{\text{Reuss}} = \left[\frac{V_{\text{soft}}}{E^*_{\text{soft}}} + \frac{1-V_{\text{soft}}}{E_{\text{CF}}}\right]^{-1}$ according to the viscoelastic correspondence principle [38]. Then, using Eq. (C.17), the total strain energy in the cell becomes

$$U_{\text{cell}} = 4U^{\text{CF}}_{\text{in-plane}} + 8U^{\text{Reuss}}_{\text{out-of-plane}} \tag{C.18}$$

By definition, $U_{\text{cell}} = \frac{1}{2}F_z\delta_z$ where F_z is the total compressive force applied to the cell in the (global) z-direction. Using this definition and Eqs. (C.17)–(C.18), we obtain

$$F_z = [\frac{8}{9}\pi E_{\text{CF}}\frac{r^2}{L_{\text{eff}}} + \frac{16}{9}\pi E^*_{\text{Reuss}}r^2(\frac{1}{L_{\text{eff}}} + \frac{12C_1r^2}{L^3_{\text{eff}}})]\delta_z \tag{C.19}$$

Note that in Eq. (C.19) C_1 should be modified as $C_1 = \left[\frac{12E_sI}{\kappa AG_{\text{Reuss}}L^2_{\text{eff}}}\right]^{-1}$, where $G_{\text{Reuss}} = \frac{E_{\text{Reuss}}}{2(1+\nu_{\text{strut}})}$, and $\nu_{\text{strut}} = \left[\frac{V_{\text{soft}}}{\nu_{\text{soft}}} + \frac{1-V_{\text{soft}}}{\nu_{\text{CF}}}\right]^{-1}$. Since $\varepsilon_z = \frac{2\delta_z}{L}$ and $\sigma_z = \frac{F_z}{WH}$ where the cell length L is $2{\cdot}L_{\text{strut}}{\cdot}\sin\theta$, the cell width W is $2{\cdot}L_{\text{strut}}{\cdot}\sin\theta$, and the cell height H is $2{\cdot}L_{\text{strut}}{\cdot}\sin\theta$, the effective modulus of the cell according to Hooke's law ($\sigma_z = E_z\varepsilon_z$) can be expressed as:

$$E^*_z = \frac{2\sqrt{2}}{9}\pi(\frac{r^2}{L_{\text{strut}}L_{\text{eff}}})[E_{\text{CF}} + 2E^*_{\text{Reuss}}(1 + 12C_1\frac{r^2}{L^2_{\text{eff}}})] \tag{C.20}$$

We observed that Eq. (C.20) reduces to an analytical expression reported in Refs. [43,44] for a case which an octet-truss unit cell is made of a homogeneous linear elastic material. Thus, this validates our analytical model is correctly developed. Finally, by definition, the intrinsic damping in terms of the loss tangent can be obtained by taking the ratio of imaginary to real parts of Eq. (C.20), that is

$$\tan\delta = \frac{\text{Im}(E^*_z)}{\text{Re}(E^*_z)} = \frac{E''_z}{E'_z} \tag{C.21}$$

Comparison between analytical model and experimental results

To investigate the analytical model-experiment agreement, the mechanical behaviors at small strains between the model and experimental results for a relative density of 7 % were compared as an example, as reported in Fig. C.2 . The model underestimates the effective modulus for V_{soft} less than 5 % and overestimated it for higher V_{soft}; however, the overall trend was predicted with a good agreement and the model predicts the modulus well

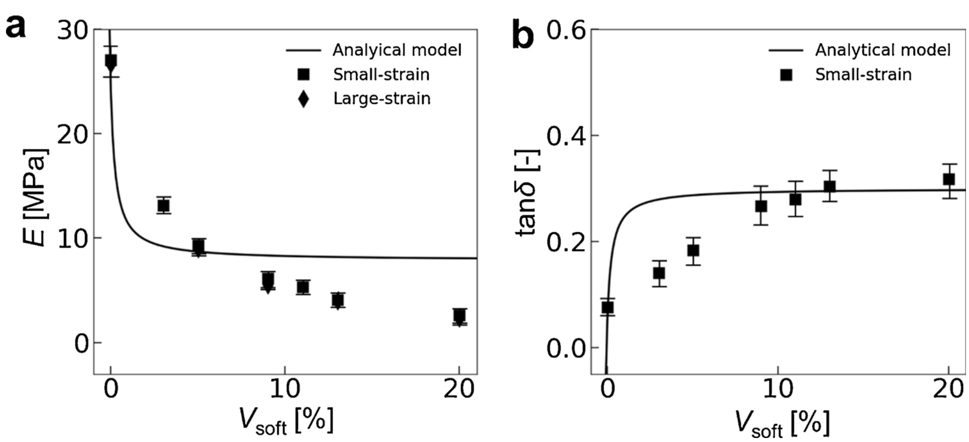

Fig. C2. Comparison between the analytical model and experimental results. (a) Modulus. (b) Intrinsic loss tangent at small strains.

Table C1
Analytical model-experiment comparison for intrinsic damping performance of lightweight cellular CFRP microlattices having a relative density of 7 % with different V_{soft}. In this table, *Avg.* and *SD* refer to the averaged value and standard deviation of the quantities of interest, respectively. FOM was computed using the averaged values of modulus and loss tangent.

Regime	V_{soft} [%]	Modulus (E) [MPa]			Loss tangent ($\tan\delta$) [-]			FOM [$\text{Pa}^{1/3}/\text{kgm}^{-3}$]	
		Experiment		Analytical model	Experiment		Analytical model	Experiment	Analytical model
		Avg.	*SD*		*Avg.*	*SD*		*Avg.*	
Small strains (intrinsic)	0	27.060	1.218	24.190	0.076	0.009	0.068	0.255	0.228
	3	13.112	0.577	9.220	0.141	0.017	0.278	0.386	0.677
	5	9.323	0.438	8.700	0.183	0.023	0.286	0.447	0.683
	9	6.130	0.294	8.330	0.267	0.028	0.292	0.568	0.687
	11	5.320	0.208	8.250	0.279	0.023	0.293	0.566	0.688
	13	4.108	0.337	8.190	0.304	0.019	0.294	0.565	0.688
	20	2.659	0.242	8.070	0.318	0.021	0.296	0.512	0.69

for V_{soft} = 0 %. As for the loss tangent, while the model predicts the intrinsic loss tangent with a rapid convergence to its asymptotic value, the experimental results show a gradual increase, however, similar trends were observed. These discrepancies are not surprising because this simple analytical model assumes no defects in the fabricated samples (e.g., the absence of fabrication imperfection) and perfect testing conditions. These samples most likely have exhibited (i) localized nodal fractures, (ii) finite-size effects, (iii) possible plastic deformation, which the model did not consider. Assumption of linear viscoelasticity in the model could be another factor contributing to these discrepancies, whereas the samples most likely have experienced some degree of nonlinearity during deformations. In addition, there was an angular misalignment of the soft phase between the model and samples. While the model assumes that the soft phase is oriented perpendicular to the axis of struts that would be seen in an ideal microlattice, the soft phase embedded in the samples is oriented parallel to print layers for a trouble-free fabrication. Although this misalignment could have contributed to the discrepancies discussed earlier, we believe that the misalignment was negligible as compared to influences from other possible causes since the total volume of the soft phase is identical between the model and the samples even with the misalignment. We emphasize that the model developed in this study intends to provide estimations of the modulus and loss tangent with an order-of-magnitude margin and to approximate their overall trends. More advanced analytical models or detailed computations are required to predict with better accuracy.

References

[1] X.Y. Zheng, H. Lee, T.H. Weisgraber, M. Shusteff, J. DeOtte, E.B. Duoss, J.D. Kuntz, M.M. Biener, Q. Ge, J.A. Jackson, S.O. Kucheyev, N.X. Fang, C.M. Spadaccini, Ultralight, ultrastiff mechanical metamaterials, Science 344 (6190) (2014) 1373–1377.

[2] R.M. Hensleigh, H.C. Cui, J.S. Oakdale, J.C.C. Ye, P.G. Campbell, E.B. Duoss, C.M. Spadaccini, X.Y. Zheng, M.A. Worsley, Additive manufacturing of complex micro-architected graphene aerogels, Mater. Horiz. 5 (6) (2018) 1035–1041.

[3] X.Y. Zheng, W. Smith, J. Jackson, B. Moran, H.C. Cui, D. Chen, J.C. Ye, N. Fang, N. Rodriguez, T. Weisgraber, C.M. Spadaccini, Multiscale metallic metamaterials, Nat. Mater. 15 (10) (2016) 1100-+.

[4] H.C. Cui, R. Hensleigh, H.S. Chen, X.Y. Zheng, Additive Manufacturing and size-dependent mechanical properties of three-dimensional microarchitected, high-temperature ceramic metamaterials, J. Mater. Res. 33 (3) (2018) 360–371.

[5] D. Chen, X.Y. Zheng, Multi-material additive manufacturing of metamaterials with giant, tailorable negative Poisson's ratios, Sci. Rep.-UK 8 (2018).

[6] L.R. Meza, A.J. Zelhofer, N. Clarke, A.J. Mateos, D.M. Kochmann, J.R. Greer, Resilient 3D hierarchical architected metamaterials, P Natl. Acad. Sci. U. S. A. 112 (37) (2015) 11502–11507.

[7] J. Bauer, L.R. Meza, T.A. Schaedler, R. Schwaiger, X.Y. Zheng, L. Valdevit, Nanolattices: an emerging class of mechanical metamaterials, Adv Mater 29 (40) (2017).

[8] E. Linul, N. Movahedi, L. Marsavina, The temperature and anisotropy effect on compressive behavior of cylindrical closed-cell aluminum-alloy foams, J. Alloys. Compd. 740 (2018) 1172–1179.

[9] L. Marsavina, D.M. Constantinescu, E. Linul, D.A. Apostol, T. Voiconi, T. Sadowski, Refinements on fracture toughness of PUR foams, Eng. Fract. Mech. 129 (2014) 54–66.

[10] F. Berto, P. Lazzarin, Recent developments in brittle and quasi-brittle failure assessment of engineering materials by means of local approaches, Mat. Sci. Eng. R 75 (2014) 1–48.

[11] D.S. Yao, H.C. Cui, R. Hensleigh, P. Smith, S. Alford, D. Bernero, S. Bush, K. Mann, H.F. Wu, M. Chin-Nieh, G. Youmans, X.Y. Zheng, Achieving the upper bound of piezoelectric response in tunable, wearable 3D printed nanocomposites, Adv. Funct. Mater. 29 (42) (2019).

[12] N.J.R.K. Gerard, H.C. Cui, C. Shen, Y.B. Xie, S. Cummer, X.Y. Zheng, Y. Jing, Fabrication and experimental demonstration of a hybrid resonant acoustic gradient index metasurface at 40 kHz, Appl. Phys. Lett. 114 (23) (2019).

[13] H.C. Cui, R. Hensleigh, D.S. Yao, D. Maurya, P. Kumar, M.G. Kang, S. Priya, X.Y. Zheng, Three-dimensional printing of piezoelectric materials with designed anisotropy and directional response, Nat. Mater. 18 (3) (2019) 234-+.

[14] R. Lakes, Viscoelastic Materials, Cambridge University Press, 2009.

[15] O.R.N. Laboratory, ORNL Develops Textile-based Carbon Fiber for Automotive Fenders, (2018) (Accessed 25 Nov 2019), https://www.ornl.gov/content/ornl-develops-textile-based-carbon-fiber-automotive-fenders.

[16] L.l.n. laboratory, Precision Effects Fielded Within Months, (2019) (Accessed 25 NOV 2019), https://manufacturing.llnl.gov/fiber-composites.

[17] O.R.N. Laboratory, 3D Printed Tool for Building Aircraft Achieves Guinness World Records Title, (2016) (Accessed 25 Nov 2019), https://www.ornl.gov/news/3d-printed-tool-building-aircraft-achieves-guinness-world-records-title.

[18] J. Xiong, R. Mines, R. Ghosh, A. Vaziri, L. Ma, A. Ohrndorf, H.J. Christ, L.Z. Wu, Advanced micro-lattice materials, Adv. Eng. Mater. 17 (9) (2015) 1253–1264.

[19] Q.Q. Wu, L. Ma, L.Z. Wu, J. Xiong, A novel strengthening method for carbon fiber composite lattice truss structures, Compos. Struct. 153 (2016) 585–592.

[20] S. Yin, J.N. Li, B.H. Liu, K.P. Meng, Y. Huan, S.R. Nutt, J. Xu, Honeytubes: Hollow lattice truss reinforced honeycombs for crushing protection, Compos. Struct. 160 (2017) 1147–1154.

[21] J. Xiong, L. Ma, A. Vaziri, J. Yang, L. Wu, Mechanical behavior of carbon fiber composite lattice core sandwich panels fabricated by laser cutting, Acta Mater. 60 (13–14) (2012) 5322–5334.

[22] H.L. Tekinalp, V. Kunc, G.M. Velez-Garcia, C.E. Duty, L.J. Love, A.K. Naskar, C.A. Blue, S. Ozcan, Highly oriented carbon fiber-polymer composites via additive manufacturing, Compos. Sci. Technol. 105 (2014) 144–150.

[23] B.G. Compton, J.A. Lewis, 3D-printing of lightweight cellular composites, Adv. Mater. 26 (34) (2014) 5930-+.

[24] J.R. Raney, B.G. Compton, J. Mueller, T.J. Ober, K. Shea, J.A. Lewis, Rotational 3D printing of damage-tolerant composites with programmable mechanics, P Natl. Acad. Sci. U. S. A. 115 (6) (2018) 1198–1203.

[25] F.D. Ning, W.L. Cong, J.J. Qiu, J.H. Wei, S.R. Wang, Additive manufacturing of carbon fiber reinforced thermoplastic composites using fused deposition modeling, Compos Part B-Eng. 80 (2015) 369–378.

[26] M.N. Jahangir, K.M.M. Billah, Y. Lin, D.A. Roberson, R.B. Wicker, D. Espalin, Reinforcement of material extrusion 3D printed polycarbonate using continuous carbon fiber, Addit. Manuf. 28 (2019) 354–364.

[27] G. Kim, E. Barocio, R.B. Pipes, R. Sterkenburg, 3D printed thermoplastic polyurethane bladder for manufacturing of fiber reinforced composites, Addit. Manuf. 29 (2019).

[28] M.S. Scholz, B.W. Drinkwater, R.S. Trask, Ultrasonic assembly of anisotropic short fibre reinforced composites, Ultrasonics 54 (4) (2014) 1015–1019.

[29] T.M. Llewellyn-Jones, B.W. Drinkwater, R.S. Trask, 3D printed components with ultrasonically arranged microscale structure, Smart Mater. Struct. 25 (2) (2016).

[30] J. Greenhall, B. Raeymaekers, 3D printing macroscale engineered materials using ultrasound directed self-assembly and stereolithography, Adv. Mater. Technol.-US 2 (9) (2017).

[31] J. Qiao, Y.R. Li, L.Q. Li, Ultrasound-assisted 3D printing of continuous fiber-reinforced thermoplastic (FRTP) composites, Addit. Manuf. 30 (2019).

[32] D. Han, C. Yang, N.X. Fang, H. Lee, Rapid multi-material 3D printing with projection micro-stereolithography using dynamic fluidic control, Addit. Manuf. 27 (2019) 606–615.

[33] X. Mu, T. Bertron, C. Dunn, H. Qiao, J. Wu, Z. Zhao, C. Saldana, H.J. Qi, Porous polymeric materials by 3D printing of photocurable resin, Mater. Horiz. 4 (3) (2017) 442–449.

[34] X. Song, Y. Chen, T.W. Lee, S.H. Wu, L.X. Cheng, Ceramic fabrication using Mask-Image-Projection-based Stereolithography integrated with tape-casting, J. Manuf. Process. 20 (2015) 456–464.

[35] X.Y. Zheng, J. Deotte, M.P. Alonso, G.R. Farquar, T.H. Weisgraber, S. Gemberling, H. Lee, N. Fang, C.M. Spadaccini, Design and optimization of a light-emitting diode projection micro-stereolithography three-dimensional manufacturing system, Rev. Sci. Instrum. 83 (12) (2012).

[36] L. Salari-Sharif, T.A. Schaedler, L. Valdevit, Energy dissipation mechanisms in hollow metallic microlattices, J. Mater. Res. 29 (16) (2014) 1755–1770.

[37] E.J. Graesser, C.R. Wong, The relationship of traditional damping measures for materials with high damping capacity - a review, Am. Soc. Test Mater. 1169 (1992) 316–343.

[38] C.P. Chen, R.S. Lakes, Analysis of high-loss viscoelastic composites, J. Mater. Sci. 28 (16) (1993) 4299–4304.

[39] H.R. Shercliff, M.F. Ashby, Elastic structures in design, Encycl. Mater. Sci. Technol. (2001) 2429–2433.

[40] L. Salari-Sharif, T.A. Schaedler, L. Valdevit, Hybrid hollow microlattices with unique combination of stiffness and damping, J. Eng. Mater.T Asme. 140 (3) (2018).

[41] A. Asadpoure, M. Tootkaboni, L. Valdevit, Topology optimization of multiphase architected materials for energy dissipation, Comput. Methods Appl. Mech. Eng. 325 (2017) 314–329.

[42] M.F. Ashby, Materials Selection in Mechanical Design, 2nd ed., Butterworth Heinemann, Oxford, 1999.

[43] V.S. Deshpande, N.A. Fleck, M.F. Ashby, Effective properties of the octet-truss lattice material, J. Mech. Phys. Solids 49 (8) (2001) 1747–1769.

[44] L. Dong, V. Deshpande, H. Wadley, Mechanical response of Ti-6Al-4V octet-truss lattice structures, Int. J. Solids Struct. 60–61 (2015) 107–124.

[45] G. Design, C.E.S. EduPack, (2018) 2019https://grantadesign.com/education/ces-edupack/ (Accessed 25 NOV 2019).